

Unveiling the vortex glass phase in the surface and volume of a type-II superconductor

Jazmín Aragón Sánchez,¹ Raúl Cortés Maldonado,¹ Néstor René Cejas Bolecek,¹ Gonzalo Rumi,¹ Pablo Pedrazzini,¹ Moira I. Dolz,² Gladys Nieva,¹ Cornelis J. van der Beek,³ Marcin Konczykowski,³ C. D. Dewhurst,⁴ R. Cubitt,⁴ Alejandro B. Kolton,¹ Alain Pautrat,⁵ and Yanina Fasano^{*1}

¹*Centro Atómico Bariloche and Instituto Balseiro, CNEA, 8400 Bariloche, Argentina.*

²*Universidad Nacional de San Luis and Instituto de Física Aplicada, CONICET, 5700 San Luis, Argentina.*

³*Laboratoire des Solides Irradiés, École Polytechnique, CNRS, 91128 Palaiseau, France.*

⁴*Institut Laue-Langevin, B.P. 156, 38042 Grenoble Cedex 9, France*

⁵*Laboratoire CRISMAT-EnsiCaen, Caen, France.*

(Dated: May 17, 2019)

Order-disorder transitions between glassy phases are quite common in nature and yet a comprehensive survey of the microscopic structural changes remains elusive since the scale of the constituents is tiny and in most cases few of them take part in the transformation. Vortex matter in type-II superconductors is a model system where some of the experimental challenges inherent to this general question can be tackled by adequately choosing the host superconducting sample. For instance, $\text{Bi}_2\text{Sr}_2\text{CaCu}_2\text{O}_{8+\delta}$ is a type-II superconductor with weak point disorder that presents a transition between two glassy phases on increasing the constituents' (vortices) density. At low vortex densities, the impact of disorder produces the nucleation of a glassy yet quasi-crystalline phase, the Bragg glass. For high vortex densities the stable phase, coined as *vortex glass*, was proposed to be disordered, but its structural properties have remained elusive up to now. Here we answer this question by combining surface and bulk vortex imaging techniques, and show that the vortex glass is neither a messy nor a hexatic phase: in the plane of vortices it presents large crystallites with positional correlations growing algebraically and short-ranged orientational order. However, no dramatic change in the correlation length along the direction of vortices is observed on traversing the order-disorder transformation.

Order-disorder structural transitions are such ubiquitous in nature that we are faced to solid-to-liquid and solid-to-solid structural transformations in everyday experience. Quite frequently, the unavoidable disorder present in the materials that are transforming favors the stabilization of glassy phases, such as spin, electric, and superconducting glass systems.¹ In order to expand the potential applications of these materials, we need to have direct access, with microscopic resolution, on the structural changes entailed at order-disorder transformations. Considerable experimental information on this issue was obtained in the solid-to-liquid case, concerning monolayers of electrons trapped on the surface of liquid He,² colloidal and hard spheres,^{3–5} plasma crystals,⁶ and superparamagnetic colloidal particles⁷. These experiments support the dislocation-mediated two-stage melting with an intermediate hexatic phase proposed by renowned theoretical developments in the case of melting in two dimensions,^{8–12} spin,⁸ and superfluid transitions.¹³ Only a handful of studies have directly probed the structural changes entailed in glass-to-glass order-disorder transitions in three dimensions.

Vortex matter in type-II superconductors is a model condensed matter system to study this general problem since the energy scales and dimensionality can be easily tuned by control parameters. The three competing energy scales governing the occurrence of order-disorder transformations are vortex-vortex repulsion, vortex-pinning interaction and thermal fluctuations, respectively controlled by magnetic field H , sample disorder, and temperature. Order-disorder transitions in

vortex matter occur since the vortex-vortex interaction tends to form an ordered triangular lattice whereas thermal fluctuations and the pinning produced by disorder in the crystal structure of the sample conspire against the stabilization of a perfect crystal.¹⁴ Some experimental works apply imaging techniques to reveal the structural changes entailed in glass-to-glass transitions in vortex matter,^{15–23} but focus on the in-plane microscopic details, i.e., at the sample surface. Other works study the structural changes along the third direction only and found that at the vortex melting²⁴ and glass-to-glass²⁵ transitions the coupling of vortices along the c -axis is depleted in the disordered phases. In order to have a comprehensive description of the problem, studies on imaging the in-plane as well as out-of-plane structural changes taking place in order-disorder transitions in vortex matter are required. Experimentally, this is quite challenging since requires the ability to image, with single-particle resolution, vortex matter at the surface and bulk of the sample. This is the question we are dealing with here.

In some superconducting glasses, as in the case of vortex matter nucleated in the extremely-layered high- T_c $\text{Bi}_2\text{Sr}_2\text{CaCu}_2\text{O}_{8+\delta}$ that we study here, a quasi-crystalline state of matter is stable at low vortex densities. This phase known as the Bragg glass presents a weak logarithmic decay of positional order and glassy dynamics.^{26,27} On increasing vortex density (magnetic field), a first-order transition towards another phase, the *vortex glass*, takes place at a characteristic field $B_{\text{ord-dis}}$.²⁸ The vortex glass is expected to present a positional order that is not quasi-crystalline, with non-divergent peaks in the

structure factor as in the case of the Bragg glass. The order-disorder transition field is frequently observed as concomitant to the onset of the so-called *second-peak effect*.^{29–32} This effect refers to the sudden enhancement or peak in the superconductor critical current when increasing field or temperature, as a consequence of pinning energy overcoming the elastic energy in the disordered phase. The $B_{\text{ord-dis}}$ transition field at which the vortex density presents a jump²⁹ coincides with the onset field of the second peak effect, B_{on} . At high temperatures the order-disorder transition continues as a first-order melting at the B_{FOT} line separating the Bragg glass and the vortex liquid phase.³³ The phase coherence along the direction of vortices is depleted both at $B_{\text{ord-dis}}$ and B_{FOT} ,²⁵ namely at the whole border of the Bragg glass phase.

Small angle neutron scattering (SANS) is a bulk-sensitive technique that allows to extract quantitative information on real space correlation lengths. For the model superconducting glass we study here, previous SANS data reveal that the vortex diffraction pattern does not significantly change on traversing the $B_{\text{ord-dis}}$,^{34,35}, but the scattered intensity was strongly reduced for $B > B_{\text{ord-dis}}$. Therefore, precise details on the structural properties of the vortex glass phase were not accessible in those works. A similar resolution-limited problem was also reported for SANS data in the vortex glass phase of other superconductors.^{27,36} Therefore, SANS experiments with improved resolution are needed to characterize the fine structural changes entailed at the glass-to-glass transformation. In this work we combine such SANS measurements with direct imaging of the $\text{Bi}_2\text{Sr}_2\text{CaCu}_2\text{O}_{8+\delta}$ vortex structure in large fields-of-view at the surface of the sample for the ordered and disordered phases. We unveil the evolution of the in-plane and longitudinal vortex correlation lengths, as well as distance-evolution of the in-plane orientational and positional order, on traversing the Bragg-to-vortex glass transition.

Results

A. Effect of point disorder on the Bragg-to-vortex glass transition

The order-disorder transition in pristine $\text{Bi}_2\text{Sr}_2\text{CaCu}_2\text{O}_{8+\delta}$ vortex matter occurs at approximately 200-300 Gauss, well above the vortex density range that can be probed by most real-space techniques that grant access to wide fields-of-view of thousands of vortices.³⁷ However, introducing extra point disorder in the samples by irradiation with electrons at low temperatures results in a significant lowering of the order-disorder line in the phase diagram.^{30,38} Such a procedure allows us to apply the magnetic decoration technique (MD)³⁹ to observe, in real space, and over large fields-of-view, the structural changes entailed at

the surface of these samples at $B_{\text{ord-dis}}$.

Our samples are pristine and electron-irradiated $\text{Bi}_2\text{Sr}_2\text{CaCu}_2\text{O}_{8+\delta}$ single crystals. During irradiation, high-energy electrons traverse the entire sample thickness, generating an almost homogeneous distribution of atomic point defects: roughly 10 % of atoms, depending on the irradiation dose, may be displaced from its initial position. The pristine samples P studied by MD are 30 small single crystals, whereas for SANS measurements we used one millimetric-large single crystal. We also study two electron-irradiated samples, A and B, first oxygen-annealed and then irradiated with 2.3 MeV electrons at 20 K, which produced a significant decrease of $B_{\text{ord-dis}}$.³⁰ Sample B has a larger irradiation dose than sample A, see Methods section. The changes in the vortex phase diagram induced by irradiation with electrons, are tracked by means of dc and ac local Hall magnetometry. Detailed data on the detection of B_{FOT} , $B_{\text{ord-dis}} = B_{\text{ON}}$, and the sweep-rate dependent B_{SP} field at which the critical current presents a peak on increasing H can be found in the Supplementary Material section.

Figure 1 shows the vortex phase diagram for pristine and electron-irradiated $\text{Bi}_2\text{Sr}_2\text{CaCu}_2\text{O}_{8+\delta}$ samples A and B. Increasing the dose of irradiation with electrons produces a systematic decrease of T_c and $B_{\text{ord-dis}}$,³⁸ and then the Bragg glass phase spans a smaller $B - T$ phase region. At low temperatures, sample A has a $B_{\text{ord-dis}} = 85(-5)$ Gauss and for sample B this value is even reduced to $\sim 40(-8)$ Gauss. The order-disorder transition field also depends on the oxygen-doping and annealing of the samples,^{30,40} and this is the reason why sample B presents the smallest reported value of $B_{\text{ord-dis}}$ obtained by electron irradiation. This allowed us to reveal the structural properties of the vortex glass phase in extended fields-of-view by means of MD.

B. Bragg-to-vortex glass transformation from real-space MD imaging

Figure 2 shows MD snapshots with more than 1500 individually-resolved vortices taken after field-cooling the samples down to 4.2 K, at different applied fields above and below B_{SP} . Changing field varies the lattice spacing of the hexagonal vortex lattice $a_0 = 1.075\sqrt{\Phi_0/B}$. Vortices are decorated with Fe particles attracted by the local field gradient generated around the cores, observed as the black dots in the inverted scanning-electron-microscopy images of Fig. 2. The decorated structures were frozen, at length scales of a_0 , at temperatures at which the pinning generated by disorder sets in.^{39,41} This freezing temperature is some K below the temperature at which magnetic response becomes irreversible,⁴² see the B_{IL} in Fig. 1 (dashed lines). For $B \leq B_{\text{ord-dis}}$ the B_{IL} line coincides with the melting line B_{FOT} within the experimental error.

Panels (a) and (b) of Fig. 2 correspond to snapshots of vortex positions taken at $B < B_{\text{ord-dis}}$ for the Bragg

glass phase. For fields larger than 15 Gauss, the vortex structure is single-crystalline and presents very few topological defects associated with non-sixfold coordinated vortices. For instance, the vortex structure of Fig. 2 (a) nucleated in a pristine sample for $B/B_{\text{ord-dis}} = 0.28$ is defectless in this field-of-view. For fields smaller than 15 Gauss, the structure breaks into small crystallites for pristine⁴³ as well as electron-irradiated samples. This polycrystalline structure results from vortex-vortex interaction weakening and disorder becoming more relevant on the viscous freezing dynamics.⁴³

Vortices are better resolved by MD in pristine than in electron-irradiated samples: at a given B , the maximum-to-background intensity of the decoration image is larger in P samples. This is in agreement with the reported increase in the superconducting penetration depth $\lambda(0)$ when irradiating with electrons.³⁸ For samples A and B, we estimate $\lambda(0)$ is 30% larger than in P samples from the difference in the entropy-jump at B_{FOT} .³⁸ An enhancement of $\lambda(0)$ results in a decrease of the local field gradient that diminishes the magnetic force attracting the Fe particles that decorate individual vortex positions. This reduces the maximum field up to which individual vortices can be resolved with MD in electron-irradiated samples, ~ 90 Gauss for samples A and B.

Nevertheless, for sample B this field is high enough as to take snapshots of the vortex glass phase in extended fields-of-view. Figure 2 shows the largest picture of the vortex glass phase that we have obtained for $B/B_{\text{ord-dis}} = 1.62$, with more than 1500 vortices. The overimposed Delaunay triangulation joining first-neighbor vortices highlights the presence of grain boundaries separating relatively large crystallites with hundreds of vortices. The orientation between crystallites changes between 20 to 30 degrees. Roughly 6% of vortices are non-sixfold coordinated and form different topological defects: 60% participate in grain boundaries (violet triangles), 19% form isolated edge dislocations (orange triangles) and the remaining 21% are involved in twisted-bond deformations (pink triangles). Isolated edge dislocations are plastic deformations entailing the nucleation of two extra vortex planes; twisted bonds are two adjacent edge dislocations with opposite Burgers vectors and do not entail any extra vortex plane. Twisted bonds are local elastic deformations that can be cured by displacing individual vortex positions in a fraction of the lattice spacing. This snapshot of the vortex glass reveals that, within a crystallite, isolated edge dislocations entail plastic deformations even at large length scales. Indeed, only $\sim 40\%$ of the observed edge dislocations are paired with their Burgers vectors pointing in opposite directions (red arrows in Fig. 2 (c)).

The proliferation of topological defects in the vortex glass phase contrasts with most of the Bragg glass phase being single-crystalline with a fraction of non-sixfold coordinated vortices $\rho_{\text{def}} < 1\%$. Figure 3 (a) shows the evolution of this fraction, ρ_{def} , as a function of $B/B_{\text{ord-dis}}$ for samples A, B and P. At low fields

$B/B_{\text{ord-dis}} \lesssim 0.01$, the vortex structure fractures into small crystallites and $\rho_{\text{def}} \sim 50\%$. On increasing field, ρ_{def} decays dramatically and stagnates below 1% for $B/B_{\text{ord-dis}} \gtrsim 0.1$, in concomitance with the observation of a single-crystalline vortex structure. This phenomenology is common to P and electron-irradiated samples, but the precise $B/B_{\text{ord-dis}}$ value at which the structure becomes single-crystalline depends on the magnitude of point disorder. For instance, for $B/B_{\text{ord-dis}} = 0.09$ the vortex structure nucleated in sample A has large crystallites whereas that in sample P is single-crystalline, see the structure factor patterns of Fig. 3 (b). These patterns result from calculating the structure factor from the individual vortex positions detected at the sample surface, namely $S_{\text{MD}}(q, \Psi) = |\tilde{\rho}(q_x, q_y)|_{z=0}^2$, with $\tilde{\rho}$ the Fourier transform of the density of vortex lines $\rho(x, y, z) = \frac{1}{t} \sum_{j=1}^N \delta(x - x_j(z)) \delta(y - y_j(z))$ with t the thickness of the sample and N the number of vortices. On increasing field above $B_{\text{ord-dis}}$, well within the vortex glass phase, the density of defects enhances up to 6.5% at $B/B_{\text{ord-dis}} = 1.62$. Within our experimental field-of-view the structure presents four large crystallites, resulting in multiple Bragg peaks in the $S_{\text{MD}}(q, \Psi)$ pattern, see Fig. 3 (b).

C. Vortex glass: fracturing into large non-hexatic domains

Theoretical studies for order-disorder transitions in two dimensions predict that between the ordered crystal and the fully disordered liquid exists an intermediate hexatic phase presenting long-range orientational and short-range positional orders.⁸ Whether this is a general scenario that also holds for three-dimensional systems will provide useful information for describing order-disorder transitions on general grounds. A seminal work for the intermediate dimensionality case of thick superconducting films reported a first-order transition to a high-field vortex state with strongly reduced longitudinal correlations, at odds with a hexatic vortex state.⁴⁴

Figure 4 shows the evolution of the orientational order at the surface of the vortex structure (from MD data) on crossing the Bragg to vortex glass transition. We characterized the orientational order by means of the correlation function $G_6(r) = \langle \Psi_6(0) \Psi_6^*(r) \rangle$ that depends on the distance-evolution of the hexagonal orientational order parameter $\Psi_6(\mathbf{r} = \mathbf{r}_i) = \sum_{j=1}^n (1/n) \exp(6i\theta_{ij})$ calculated from the bond angles of nearest neighbor vortices i and j , θ_{ij} . For $B/B_{\text{ord-dis}} \leq 0.1$, G_6 starts decaying algebraically at short distances (see dashed lines) up to a characteristic length of the order of the size of the crystallites, see arrows. For larger distances the decay of G_6 is fitted by an exponential dependence. On further increasing field within the Bragg glass ($0.1 < B/B_{\text{ord-dis}} < 1$), single crystalline vortex structures are observed and coincidentally G_6 decays algebraically at all distances. The field-evolution of the exponent η of this algebraic decay

is shown in Fig. 4 (c) for pristine and electron-irradiated samples: it decreases dramatically when passing from the polycrystalline to the single-crystalline structures and remains almost constant for $B/B_{\text{ord-dis}} > 0.2$. This stagnation is expected for a phase presenting long-range orientational order such as the Bragg glass. Interestingly, the saturation value $\eta \sim 0.025$ that we found at the surface of the vortex structure nucleated in the Bragg glass phase is roughly one order of magnitude smaller than the value found in the same phase from bulk SANS measurements in single-crystalline vanadium.²³ This indicates that vortex meandering within the sample thickness is significant even though the orientational order of the Bragg glass is long-ranged in the whole sample volume.

For fields above $B_{\text{ord-dis}}$, the vortex glass phase presents a faster decay of orientational order: even within the larger crystallite of the center of Fig. 2, G_6 decays exponentially with distance. Once the limits of the grain boundary are reached, see black arrow in Fig. 4 (a), there is a kink in G_6 and the decay continues to be exponential. Therefore, the orientational order of the vortex glass phase at the surface of $\text{Bi}_2\text{Sr}_2\text{CaCu}_2\text{O}_{8+\delta}$ samples is not characterized by the typical algebraic decay of a hexatic phase. This goes at odds with theories of the vortex glass being an hexatic phase,⁴⁵ but is evocative of another theoretical proposals of a multi-domain glassy phase separating the Bragg glass and the vortex liquid.⁴⁶ The fracturing of the vortex structure into large domains in the vortex glass phase could be a non-equilibrium feature, due to finite cooling rates during the nucleation of the structure in field-cooling experiments.³⁶ Nevertheless, the vortex glass presents non-hexatic order already inside the crystallites.

Data from SANS experiments probing the structural properties of the vortex glass in the whole thickness of the sample are consistent with this degradation of orientational order at the surface. The intensity measured in a SANS experiment is the product of the structure factor times the magnetic form factor $f(q)$ averaged over the entire volume of the sample, $I(q) = S_{\text{SANS}}(q, \Psi) \cdot f^2(q)$.³⁵ The structure factor measured in SANS therefore collects information on the meandering of vortices along the sample thickness, namely $S_{\text{SANS}}(q, \Psi) = |\int \rho(q_x, q_y, z) dz|^2$. Figure 5 shows a comparison of the physical magnitudes that can be accessed in SANS and MD experiments showing data obtained in the Bragg and vortex glass phases of $\text{Bi}_2\text{Sr}_2\text{CaCu}_2\text{O}_{8+\delta}$.

Figure 6 shows the field-evolution of the SANS intensity $I(q_{\text{Bragg}}) \cdot q_{\text{Bragg}}$ measured at the Bragg wave-vector $q_{\text{Bragg}} = 2\pi/a_0$ and normalized by its value at zero field, for pristine $\text{Bi}_2\text{Sr}_2\text{CaCu}_2\text{O}_{8+\delta}$. In the London limit when vortices are sufficiently separated (see Supplementary material for discussion on the validity of this limit), this magnitude is field-independent only if S_{SANS} is constant. The figure also includes previous data from (K, Ba)BiO₃, considered in the literature as decisive to confirm experimentally that the phase at

$B < B_{\text{ord-dis}}$ is the Bragg glass.²⁷ Similarly as in our case, the authors of Ref. 27 considered $B_{\text{ord-dis}} = B_{\text{ON}}$, the onset field of the second peak effect measured in (K, Ba)BiO₃. For $B/B_{\text{ord-dis}} < 1$, the data for both systems are remarkably similar within the instrumental resolution of each experiment. For both materials the neutron intensity $I(q_{\text{Bragg}}) \cdot q_{\text{Bragg}}$ is field-independent for $B \lesssim 0.4B_{\text{ord-dis}}$ and decreases roughly exponentially beyond $0.4B_{\text{ord-dis}}$. Therefore, our results in the low-field phase of $\text{Bi}_2\text{Sr}_2\text{CaCu}_2\text{O}_{8+\delta}$ are consistent with the phenomenology observed in the Bragg glass phase of (K, Ba)BiO₃.

In the vicinity of the glass-to-glass transition, the normalized SANS intensity is of the order of 0.1 in both systems. For the measurements in (K, Ba)BiO₃ of Ref. 27 the authors stated that the intensity was below the noise level for $B \sim B_{\text{ord-dis}}$ and beyond. In our measurements we are able to detect a measurable intensity in the vortex glass phase since we have roughly a two orders of magnitude gain in the neutron flux with respect to previous works, due to the virtuous combination of measuring a larger sample and increasing significantly the counting time. We are able to detect a non-negligible normalized neutron intensity of 6×10^{-2} well above the order-disorder transition. This experimental resolution allowed us to explore the structural properties of the vortex glass phase in $\text{Bi}_2\text{Sr}_2\text{CaCu}_2\text{O}_{8+\delta}$. We find that in the vortex glass the neutron diffracted intensity also continues to decay with field, roughly exponentially, in almost two decades more. For the field-range of our measurements in $\text{Bi}_2\text{Sr}_2\text{CaCu}_2\text{O}_{8+\delta}$, vortices are in the London limit approximation and $f(q_{\text{Bragg}}) \cdot q_{\text{Bragg}}$ is constant with field, see discussion in Supplementary material.³⁵ Therefore the decay of $I(q_{\text{Bragg}}) \cdot q_{\text{Bragg}}$ in the vortex glass of $\text{Bi}_2\text{Sr}_2\text{CaCu}_2\text{O}_{8+\delta}$ comes from a reduction of S_{SANS} with field. This implies that, undoubtedly, there is a worsening of the structural properties in the vortex glass phase of $\text{Bi}_2\text{Sr}_2\text{CaCu}_2\text{O}_{8+\delta}$.

When measuring in Bragg condition in the plane of the detector, six large diffraction peaks are always observed in the vortex glass phase, even up to $B/B_{\text{ord-dis}} = 1.8$. However, the average azimuthal width of the peaks grows on increasing field. In order to quantify the degradation of orientational order in the bulk of the vortex structure, we measure the average azimuthal width of the Bragg peaks σ_{\perp}^2 (in units of \AA^{-1}), see the $I(\Psi, q_{\text{Bragg}})$ profile in Fig. 5 (b). Correcting by the instrumental resolution we estimate the in-plane azimuthal correlation length $\xi_{\perp} = 1/(\sqrt{\sigma_{\perp}^2 - \sigma_{\perp, \text{inst}}^2})$. This magnitude is associated with the typical distance at which the shear displacements of vortices in the volume of the sample are of the order of a_0 .⁴⁷ Figure 7 (b) shows that the normalized ξ_{\perp}/a_0 obtained from SANS experiments in sample P decreases with field in the Bragg glass phase up to $B/B_{\text{ord-dis}} \sim 0.6$; then remains constant or slightly recovers (difficult to ascertain within the experimental error) up to $B_{\text{ord-dis}}$, and finally systematically decreases with field in the vortex glass. This comes from an az-

imutual widening of the Bragg peaks that is in agreement with MD evidence of a fracturing of the vortex structure into large crystallites with small misalignment, and non-hexatic orientational order inside them.

In order to quantitatively support this agreement, MD data can also be analyzed in a similar fashion as to obtain the in-plane azimuthal correlation length of the vortex structure at the sample surface. The results after analyzing the azimuthal width of the Bragg peaks observed in $S_{\text{MD}}(q, \Psi)$, corrected by the MD instrumental resolution (see details in the caption of Fig. 5) are shown with full circles in Fig. 7 (b). Turning on field from zero to $B/B_{\text{ord-dis}} \sim 0.1$, ξ_{\perp}/a_0 enhances for both pristine (black dots) and electron-irradiated (blue dots) samples. For these low fields not covered by our SANS experiments, the polycrystalline vortex matter observed by MD presents larger crystallites on increasing vortex density. Then for the range of fields where MD and SANS data are both available, the perpendicular correlation length obtained in MD experiments decreases and seems to stagnate with B within the Bragg glass phase. On the vortex glass phase, ξ_{\perp}/a_0 is slightly smaller than in the Bragg glass. The absolute value of this correlation length obtained in MD experiments is larger than in SANS, and therefore the described evolution is pictorially less evident in a semi-log plot as that of Fig. 7 (b). This difference in absolute values can not be ascribed to the form factor of vortices since this magnitude is roughly constant with field for $\text{Bi}_2\text{Sr}_2\text{CaCu}_2\text{O}_{8+\delta}$ at the studied field range. Therefore, the difference comes from the inequality between the structure factors probed by MD and SANS, the latter integrating the meandering of vortices along the sample thickness, the former having information only from the location of vortices at the surface. In addition, the SANS signal is collected in a larger sample whereas MD data are obtained in one order of magnitude smaller fields of view and the cumulative effect of topological defects in decreasing the correlation lengths is smaller.

D. Shortening of the positional order of the vortex glass

Further quantitative characterization of the structural changes at the glass-to-glass vortex transition can be gained by analyzing the functional decay of the positional order as well as the radial in-plane and longitudinal correlation lengths at the volume of the sample. Theoretically, elastic approaches showed that even though a weak random disorder destroys the perfectly hexagonal vortex structure, in the Bragg glass phase, quasi long-range in-plane positional order and algebraically divergent Bragg peaks in the structure factor are expected in the volume of the sample.²⁶ Experimentally, previous data for pristine samples show resolution-limited fine Bragg peaks^{27,35}, and images at the surface reveals a distance-evolution of the positional correlation function³⁹

and displacement correlator⁴⁸ consistent with the random manifold regime of the Bragg glass. In this section we focus on the positional order characteristic of the vortex glass phase hinging our analysis on physical magnitudes that were also used to fingerprint the Bragg glass phase.

In particular, a relevant magnitude to describe the positional order is the displacement correlator, $W(r) = \langle [u(r) - u(0)]^2 \rangle / 2$ with $u(r)$ the displacement of vortices with respect to the sites of a perfect hexagonal lattice, and the average taken over quenched disorder and thermal fluctuations. This magnitude can in principle be obtained from MD data, but computing $W(r)$ for structures with topological defects as observed experimentally is not straightforward. Following a previous work of some of us, we implemented an algorithm to locally calculate $W(r)$ in structures with defects.⁴⁹ The comparison is not done with a unique perfect hexagonal structure in the whole field-of-view, but instead with local perfect lattices with lanes oriented in the three principal directions of the local structure. The regional lanes stop running two lattice parameters away of any topological defect and new lanes are defined if the structure slightly modifies its orientation. Using this local algorithm, we obtain a modified average displacement correlator $W^*(r)$ for structures with topological defects. The Supplementary material section includes a schematics on how this analysis is performed.

Figure 4 (b) presents the distance-evolution of W^*/a_0^2 for various $B/B_{\text{ord-dis}}$ ratios on traversing the order-disorder transition for electron irradiated samples A and B. The main panel of Fig. 4 (b) shows that for $B/B_{\text{ord-dis}} < 1$, $W^*/a_0^2 \propto (r/a_0)^\nu$, see fits presented with dashed lines. The same phenomenology is observed in the Bragg glass phase of P samples studied here, see the Supplementary material section. The exponent ν for both electron-irradiated and pristine samples decays with $B/B_{\text{ord-dis}}$ in the Bragg glass phase, see Fig. 4 (c). For P samples ν stagnates for $B/B_{\text{ord-dis}} > 0.2$ around the value of 0.44 indicated with a dotted line in the figure. The algebraic decay of W^*/a_0^2 , as well as this value of ν , are theoretically expected for the random-manifold regime of the Bragg glass.⁵⁰ Even for the case of the polycrystalline vortex structures observed at $B/B_{\text{ord-dis}} \leq 0.1$, the growth of W^*/a_0^2 follows the same functionality inside the crystallites (distances below the arrow in Fig. 4 (b)). In contrast, for electron irradiated samples, ν does not seem to stagnate for the studied fields, but reaches a value of ~ 0.5 for $B/B_{\text{ord-dis}} = 0.75$. These values of ν for the Bragg glass phase are roughly one order of magnitude larger than those found for describing the decay of orientational order, η , indicating bond orientational order in the Bragg glass phase is of longer range, as compared to translational order.

For the vortex glass phase, the growth of W^*/a_0^2 can still be fitted with an algebraic growth, but the exponent found, $\nu = 0.7$, is significantly larger than in the Bragg glass. This behavior is found already at distances smaller than the typical crystallite size in the vortex glass phase,

see data in the insert to Fig. 4 (b) for $B/B_{\text{ord-dis}} = 1.62$ with a crystallite size of $\sim 20a_0$. In addition, also the absolute value of the cumulated displacements at a fixed distance changes on traversing the order-disorder transition. For instance, Fig. 4 (d) shows the evolution of W^*/a_0^2 at $r/a_0 = 10$ with increasing field: in the Bragg glass phase decreases up to $B/B_{\text{ord-dis}} = 0.2$, roughly stagnates up to the order-disorder transition, and has a significantly larger value in the vortex glass phase. All this evidence suggests that the vortex glass presents short-range positional order with $u(r)$ growing faster than in the Bragg glass phase.

We further characterized the nature of the positional order of the vortex glass by studying the correlation lengths in the volume of the sample from SANS data. The first magnitude that we study is the radial in-plane correlation length ξ_{\parallel} , associated with compressive displacements of the vortex structure convoluted all along the thickness of the sample. This magnitude is estimated from the radial width of the Bragg peaks minus the instrumental resolution, namely $\xi_{\parallel} = 1/\sqrt{\sigma_{\parallel}^2 - \sigma_{\parallel \text{inst}}^2}$, see Fig. 5 (b). The average q -width of the Bragg peaks, σ_{\parallel} , is only slightly larger than the experimental resolution in the Bragg glass, but for $B > B_{\text{ord-dis}}$ dramatically increases with field far beyond the instrumental resolution, see Fig. 6 (b). First, this implies that diffraction peaks in the vortex glass phase are not resolution-limited as in the Bragg glass, but widen beyond resolution. Second, the drastic widening of the peaks yields a systematic reduction of the in-plane radial correlation length with field, even in units of a_0 , as shown in Fig. 7 (a). The data for sample P obtained with SANS are consistent with the reduction of ξ_{\parallel} in units of a_0 also observed in MD data at the surface of pristine and electron-irradiated samples. Similarly as in the case of the azimuthal in-plane correlation length, MD data are generally above the SANS data since the latter convolute information in the volume of the sample. Comparative examples of the radial width of Bragg peaks in MD and SANS data, indicating the instrumental resolution in both experiments, are shown in the Supplementary material.

We get extra information on the structural properties along the direction of vortices by measuring SANS rocking curves tilting the sample around the ω direction in the Bragg condition, see Fig. 5 (b). The width of the rocking curve, once corrected by the instrumental resolution, provides an estimation of the longitudinal correlation length associated with tilting displacements, $\xi_L = 1/\sqrt{\sigma_{\omega}^2 - \sigma_{\omega \text{inst}}^2}$. This characteristic length measures the correlation along flux lines and is reached at a z -position where the lateral displacement of a vortex with respect to a straight line is of the order of coherence length. Previous results in (K,Ba)BiO₃ indicated that in the Bragg glass phase the width of the rocking curve is resolution-limited (remains roughly constant), at least within an experimental resolution of $\Delta\omega \sim 0.18$ degrees.²⁷

In our measurements in Bi₂Sr₂CaCu₂O_{8+ δ} , with an experimental resolution of $\Delta\omega \sim 0.1$ degrees, the corrected width of the rocking curve is not changing appreciably in the Bragg glass up to $B/B_{\text{ord-dis}} \sim 0.6$. However, very close to the order-disorder transition, at $B/B_{\text{ord-dis}} \sim 0.8$, the rocking curve shrinks and ξ_L/a_0 increases around 30%. On entering the vortex glass phase, the longitudinal correlation length seems to smoothly decrease, although error bars are quite large since the diffracted intensity decreases exponentially with field. Nevertheless, we have sufficient instrumental resolution as to ascertain that no dramatic collapse of ξ_L/a_0 is observed in the vortex glass phase. The shortening of the positional order in the vortex glass is more dramatic for in-plane displacements than for longitudinal ones. The latter does not rule out the possibility that some screw dislocations could nucleate along the direction of vortices in the vortex glass. These are very relevant findings since they suggest that the long-range order of the superconducting phase is maintained in the vortex glass. Indeed, Josephson plasma resonance data show that in the vortex glass the c -axis correlations are enhanced with respect to the vortex liquid.²⁵ As a consequence, our results imply, as proposed by other groups,⁵¹⁻⁵³ that superconducting phase coherence should be destroyed in a transition line between the vortex glass and the vortex liquid.

In an elastic description of the vortex lattice the ratio between the longitudinal and in-plane correlation lengths are proportional to the tilting energy, namely $\xi_L/\xi_{\perp,\parallel} \sim \sqrt{c_{44}/c_{66}}$.¹⁴ To evaluate this ratio in the case of Bi₂Sr₂CaCu₂O_{8+ δ} with $\lambda = 210^{-5}$ cm, we first consider that $c_{44} = B^2/4\pi(1 + \lambda^2 k^2) \approx B^2/4\pi$ since we are taking into account elastic distortions with $k \sim 1/\xi_L \sim 10^{-4}$ cm, and then $\lambda^2 k^2 \sim 10^{-2} \ll 1$. Second, considering the value of λ for this material and $\Phi_0 = 2.07 \cdot 10^{-7}$ G.cm² the shear elastic constant $c_{66} \approx \Phi_0 B / (8\pi\lambda)^2 \sim B$. These considerations yield $\sqrt{c_{44}/c_{66}} \simeq \sqrt{B/4\pi}$ in an elastic description for Bi₂Sr₂CaCu₂O_{8+ δ} . The insert to Fig. 7 (c) shows the field-evolution of the longitudinal (and radial) to azimuthal correlation lengths as measured by SANS. Within the error bars, these ratios are very close to $\simeq \sqrt{B/4\pi}$. This suggests that the eventual density of screw dislocations is not as large as to plastic deformations along the direction of vortices being dominant in the vortex glass.

I. DISCUSSION

The decrease of the three correlation lengths (not so dramatic for ξ_L) on transiting in the vortex glass, detected both via MD and SANS, is accompanied by a reduction of the diffracted intensity $I(q_{\text{Bragg}}) \cdot q_{\text{Bragg}}$. This intensity starts decaying for $B/B_{\text{ord-dis}} \sim 0.4$ and close to the order-disorder transition registers one decade of decrease. Although this quantitative evolution was also found in SANS measurements in (K,Ba)BiO₃

and in $(\text{Ba,K})\text{Fe}_2\text{As}_2$, in our SANS experiments in $\text{Bi}_2\text{Sr}_2\text{CaCu}_2\text{O}_{8+\delta}$, we still have a good instrumental resolution for $B > B_{\text{ord-dis}}$. In our case, this collapse is mainly due to a falling down of the structure factor $S_{\text{SANS}}(q, \Psi)$ since for the studied fields the form factor is roughly field-independent. The concomitant widening of the Bragg peaks and collapse of diffracted intensity measured by SANS at the volume are consistent with the non-hexatic vortex glass that fractures into large crystallites with small misalignment and presents a shortening of positional order as revealed at the surface by MD. These results in $\text{Bi}_2\text{Sr}_2\text{CaCu}_2\text{O}_{8+\delta}$ are consistent with SANS data in the pnictide material $(\text{Ba,K})\text{Fe}_2\text{As}_2$.³⁶ Therefore, in this particular order-disorder transition no two-stage structural transformation is detected.

The vortex system in this extremely layered superconductor undergoes a first-order glass-to-glass transition between a quasi-crystalline Bragg glass to a non-hexatic and short-range positionally ordered vortex glass with no dramatic loss of correlation along the direction of vortices. Strikingly, we obtain our results in an extremely layered type-II superconductor with flux lines formed by columns of two-dimensional pancake vortices that are longitudinally weakly-bounded, specially at high temperatures. The slight decay of ξ_L/a_0 , remaining non-negligible for $B/B_{\text{ord-dis}} > 1$, rules out the possibility of the vortex glass being a phase of decoupled pancake vortices along the field direction. Moreover, since the ratio between the longitudinal and in-plane correlation lengths follows quite well the prediction for an elastic description of the vortex glass, the proliferation of screw dislocations along the direction of vortices seems to be unlikely. Therefore, our evidence suggests that in the vortex glass phase of $\text{Bi}_2\text{Sr}_2\text{CaCu}_2\text{O}_{8+\delta}$, even though this material is extremely layered, the flux lines behave as three-dimensional, formed by coupled pancake vortices along the c-axis direction. This might be at the origin of the glass-to-glass transition in $\text{Bi}_2\text{Sr}_2\text{CaCu}_2\text{O}_{8+\delta}$ not being well described by the two-stage melting description.⁸ Therefore our results reminds that ubiquitous order-disorder transitions in nature, either melting or glass-to-glass, are richer than the scenario predicted by this theory for melting in two-dimensions. In particular, the dimensionality of vortex matter controlled by the electronic anisotropy of the host superconductor plays a determinant role in the structural properties of the disordered vortex glass phase.

Even though our results are a comprehensive study of the structural properties of the vortex glass in the surface and volume of the vortex ensemble, we surveyed these properties in a static condition after field-cooling. However, we have to have always in mind that structural transitions in vortex matter, and in systems with substrate disorder in general, are actually transitions in a state of matter different from a solid or a liquid, particularly regarding their dynamical properties. Experiments probing the dynamics of both glassy phases are thus important to further confirm our findings.

Methods

Sample preparation

We studied electron-irradiated as well as pristine $\text{Bi}_2\text{Sr}_2\text{CaCu}_2\text{O}_{8+\delta}$ samples from different sample growers. Pristine optimally-doped samples used in MD experiments (roughly 30 small single crystals) were grown, annealed and characterized at both, the Low Temperature Lab of Bariloche, Argentina, and the Kamerlingh Onnes Lab at Leiden, The Netherlands. SANS experiments were performed using a large single crystal of $30 \times 5 \times 1.2 \text{ mm}^3$ grown at the International Superconductivity Technology Center of Tokyo, Japan, by A. Rykov, and characterized at Ensicaen, France. The slightly-overdoped electron-irradiated samples (grown in a 200 mbar O_2 atmosphere at Leiden) were irradiated with 2.3 MeV electrons at low temperatures (20 K) in a van de Graaff accelerator coupled to a closed-cycle hydrogen liquifier at the École Polytechnique of Palaiseau, France.³⁸ Two single crystals with a significant decrease of the $B_{\text{ord-dis}}$ order-disorder transition field were selected for the MD study. Sample A was annealed at 793 C in air and then irradiated with a dose of $1.7 \times 10^{19} \text{ e/cm}^2$; sample B was not annealed and irradiated with $7.4 \times 10^{19} \text{ e/cm}^2$. Electrons traverse the whole sample thickness generating a roughly homogeneous distribution of point defects in the crystal structure. Irradiating at temperatures lower than the threshold temperature for defect migration is essential in order to prevent the agglomeration of defects. Some of the point defects annihilate on warming the samples, but the remaining defects are of atomic size.³⁸

Local Hall magnetometry

We applied local Hall probe magnetometry in order to track the changes produced in the vortex phase diagram by the point-defect potential introduced by electron irradiation. The local stray field of the samples is measured with an array of GaAs/AlGaAs Hall probes with active areas of $16 \times 16 \mu\text{m}^2$.⁵⁴ We performed dc and ac measurements applying constant, H , and ripple, h_{ac} , fields parallel to the c-axis of the samples. Measuring the sample magnetization, $H_s = B - H$, when cycling H at fixed temperatures allow us to obtain dc magnetic hysteresis loops as shown in Fig. 8 (a). ac transmittivity measurements are performed by simultaneously acquiring the first and third harmonics of the ac magnetic induction when applying a ripple h_{ac} field either by changing temperature at fixed H or cycling H at fixed temperature. The transmittivity T' is obtained by normalizing the in-phase component of the first-harmonic signal B' , namely $T' = [B'(T) - B'(T \ll T_c)] / [B'(T > T_c) - B'(T \ll T_c)]$.⁵⁵ This magnitude is extremely sensitive to discontinuities in the local induction as the B -jump produced at the first-order vortex transition at B_{FOT} . The third harmonic signal, $|T_{h3}| = |B_{h3}^{\text{AC}}| / [B'(T > T_c) - B'(T \ll T_c)]$, is measured to detect the onset of non-linearities in the magnetic response, see Fig. 8 (d). ac measurements were typically performed with ripple fields of 1 Oe amplitude and 7.1 Hz

frequency. Further details are discussed in the Supplementary material section.

Magnetic decoration

In order to directly image individual vortex positions in a typical field-of-view of 1000-5000 vortices, MD experiments were performed simultaneously in electron-irradiated and pristine $\text{Bi}_2\text{Sr}_2\text{CaCu}_2\text{O}_{8+\delta}$ samples. The structural properties of vortex matter were imaged below and above the B_{SP} order-disorder transition by field-cooling the samples from room temperature down to 4.2 K at applied fields $5 < H < 150$ Oe. Further details in the decoration protocol followed in this case can be found in Ref.⁴³. Magnetic decorations were performed at different fields in roughly 30 pristine freshly-cleaved small single crystals from two sample growers. For every field, experiments were performed at several realizations for statistical purposes. In the case of the two electron-irradiated samples, experiments were performed at different fields on subsequently cleaving the samples. Since this is a destructive process, every sample was first studied with Hall magnetometry and then decorated.

Small angle neutron scattering

SANS experiments were performed at the D22 diffractometer of the Institut von Laue Langevin at Grenoble, France. The wavelength of incident neutrons was of 9 and 15 Å with a wavelength resolution of 10 %. The collimation of the incident beam produced a beam divergence of $\delta(2\theta)_{\text{div}} \sim 0.1 \times 10^{-3}$ rad. The angular distribution of the scattered intensity, $I(q, \Psi)$, was measured in a $102.4 \times 98 \text{ cm}^2$ detector with 1280×1225 pixel² ($0.8 \times 0.8 \text{ mm}^2$ per pixel) located at 17.6 m from the sample. SANS data were obtained by rocking horizontally (ϕ direction) and vertically (ω direction) the whole sample and magnet system when aligned in the Bragg condition.³⁵ In order to obtain the signal coming purely from the vortex lattice, we subtracted from the raw data the normal-state background signal measured at zero field and 10 K. Similarly as in MD experiments, vortex diffraction patterns and rocking curves were measured at 4.2 K after field-cooling the sample in a magnetic field applied along the c-axis and with magnitude ranging 100 to 1000 Oe.

II. SUPPLEMENTARY MATERIAL

A. First-order transition and irreversibility line from ac and dc Hall magnetometry

The first-order high-temperature B_{FOT} and order-disorder $B_{\text{ord-dis}}$ transitions, as well as the irreversibility line of vortex matter for the studied samples were obtained combining ac and dc local magnetometry measurements. Figures 8 (a) to (d) show these results in the illustrative case of sample B. The glass-to-glass transition is detected from the onset of the local H_{S} -peaks in the ascending and descending branches of dc magnetization loops measured at low temperatures, see Fig. 8 (a).

These peaks start to develop at B_{ON} considered as the order-disorder transition field $B_{\text{ord-dis}}$; the local maxima in magnetization occurs at the field indicated as B_{SP} that unlike B_{ON} depends on the field sweep-rate. Assuming a Bean field-profile inside the sample, the critical current at a given temperature can be estimated as proportional to the separation between the ascending and descending branches of the magnetization loop. The result of this analysis is shown in Fig. 8 (b): the B_{ON} field coincides with the start of the J_{c} peak and at B_{SP} the local maximum in critical current is developed. This phenomenology for the detection of $B_{\text{ord-dis}}$ is consistent with the one followed in the literature for pristine as well as electron-irradiated $\text{Bi}_2\text{Sr}_2\text{CaCu}_2\text{O}_{8+\delta}$ samples.^{30,54}

The glass-to-glass $B_{\text{ord-dis}}$ line is the continuation of the high-temperature solid-to-liquid vortex transition H_{FOT} ,²⁹ and since both are of first order, a jump on B is observed when controlling H . Since this transition is of first-order, a jump in B is observed when controlling H . h_{ac} transmittivity is a normalized derivative of the in-phase component of the first harmonic of B . Therefore, at high temperatures the transition is observed as a paramagnetic peak in $T'(B)$,⁵⁴ as for instance shown in Fig. 8 (c). In all the studied samples, the field-position of the paramagnetic peak is independent of the frequency and amplitude of h_{ac} . For the studied samples, the slope of the $B_{\text{FOT}}(T)$ line is not dramatically altered by electron irradiation, but since the T_{c} is significantly affected the vortex solid phase spans a smaller region on increasing the irradiation dose.

We also studied the irreversibility line, a crossover line at which pinning sets in and the magnetic response becomes therefore irreversible. This is also observed as a non-linear magnetic response, namely as a non-negligible value of the higher harmonics of the ac magnetization signal. We therefore followed the standard procedure of measuring the phase location of B_{IL} from the onset of the third harmonic signal, $|T_{\text{h}3}|$.⁵⁴ Figure 8 (d) shows that on decreasing temperature $|T_{\text{h}3}|$ overcomes the typical noise level at a characteristic temperature indicated as T_{IL} and then a peak-like structure develops on further cooling. These data are shown for the illustrative case of sample B but sample A and the pristine samples follow the same phenomenology.⁵⁴ The irreversibility line is not a transition but a pinning crossover line and therefore strongly depends on the amplitude and frequency of the ripple field applied to measure ac magnetization.⁵⁴ The data shown in Fig. 8 (d) were obtained for an h_{ac} of 1 Oe and 7.1 Hz.

B. SANS intensity as a function of field: validity of the London approximation for the form factor

The decrease of $I(q_{\text{Bragg}}) \cdot q_{\text{Bragg}}$ for fields larger than $B/B_{\text{ord-dis}} = 0.4$ was proposed in Ref. 27 as due to the proliferation of topological defects on approaching $B_{\text{ord-dis}}$. Our MD and SANS results in

$\text{Bi}_2\text{Sr}_2\text{CaCu}_2\text{O}_{8+\delta}$ considered together, indeed show that there is a worsening of the structural properties of vortex matter on approaching $B_{\text{ord-dis}}$, and that the in-plane and longitudinal correlation lengths become significantly smaller in the vortex-glass phase, surely associated with the observed proliferation of defects in MD images. Nevertheless, the significant decrease of the neutron signal in the case of (K, Ba)BiO₃ can be mainly associated with a decrease of the magnetic form factor. Even for a perfect lattice in which the structure factor is equal to 1, the magnitude $I(q_{\text{Bragg}}, q_{\text{Bragg}})$ can be considered constant only in the London limit in which vortices are far apart. However, on increasing field close to H_{c2} the London limit is no longer valid and the measured intensity for a perfect lattice decreases just because the magnetic form factor of the vortex structure decreases with field. For instance, and for the case of large κ materials as studied here, Brandt showed in Ref. 56 that the neutron diffracted intensity in a Ginzburg-Landau model significantly decreases with field even for $B \sim 10^{-2} B_{c2}$.

Considering the data of Table 1 of Ref. 56, and the London expression for the neutron diffracted intensity, we plot in Fig. 9 the ratio between the neutron intensity in a Ginzburg-Landau to a London model. We have also added gray regions indicating the range of fields at which SANS measurements were performed for the two discussed type-II superconductors. Clearly our measurements in $\text{Bi}_2\text{Sr}_2\text{CaCu}_2\text{O}_{8+\delta}$ lie in the B/B_{c2} range in which the neutron diffracted intensity can be reasonably well approximated by the London model, and any decrease of intensity can only have origin in a worsening of the structure factor. However, in the case of the field-range of the SANS measurements of Ref. 27 in (K,Ba)BiO₃, the reduction in the neutron diffracted intensity can also have origin in the decrease of the magnetic form factor with field, for the field range studied in that work.

C. MD structure factor at the surface and SANS intensity in the bulk of vortex matter

Figure 10 shows q -profiles of the Bragg peaks as detected from the structure factor measured by MD (full symbols) at the sample surface and the SANS intensity (open symbols) convoluting information along the whole sample thickness. Data in the left panel shows the case of the Bragg glass phase whereas data at the vortex glass phase are presented in the right panel. The gray boxes highlight the experimental resolution for SANS and the dark gray ones for MD experiments. The SANS instrumental resolution is given mainly by the dispersion in the wavelength of neutrons and the divergence of the neutron beam on the detector. The MD resolution is estimated from considering the error in digitalizing vortex positions (depending on the number of pixels per microns of a given image), plus the typical width of the Bragg peak of a perfect lattice with the same number of vortices in a region

imaged with the same amount of pixels than in the experiment.

D. The lanes algorithm to calculate W^* in a structure with topological defects

The positional correlator was calculated using the algorithm of lanes that allow us to calculate $W^*(r)$ in the case of lattices with topological defects. The classical way to calculate the displacement correlator is to measure the transversal, u_t , and longitudinal, u_l , displacements of a vortex with respect to the nearest site of a perfect hexagonal structure oriented in a fixed direction in the whole image. This direction is obtained from the location of the peaks in the Fourier transform of the experimental structure. However, the presence of topological defects locally alters the orientational order of the structure, and if defects proliferate, the three vortex lanes of the structure can significantly change their orientation. In this case, comparing with the sites of a perfect structure with fixed orientation is not a proper way of calculating the displacement correlator since orientational information is entangled with the positional one.

We solved this problem by considering a local perfect lattice whose three lanes are defined from the local orientation of the experimental structure. Therefore the orientation of the three lanes of the perfect structure, \mathbf{a}_i with $i = 0, 1, 2$ changes when a topological defect is reached. Once these lanes are locally defined, the longitudinal u_L^i and transversal u_T^i displacements are measured to obtain $W_T^i(r) = \langle [u_T^i(r) - u_T^i(0)]^2 \rangle$ and $W_L^i(r) = \langle [u_L^i(r) - u_L^i(0)]^2 \rangle$. Then $W_T(r)$ and $W_L(r)$ are obtained by averaging the $W_T^i(r)$ and $W_L^i(r)$ measured with respect to every lane direction \mathbf{a}_i . Finally, the average displacement correlator is computed as $W^* = (W_T + W_L)/2$. An example of this analysis with the local lanes is shown in Fig. 11. The results are shown with error bars corresponding to the dispersion in W^* values for every r/a_0 .

E. Orientational and positional order of the Bragg glass in pristine $\text{Bi}_2\text{Sr}_2\text{CaCu}_2\text{O}_{8+\delta}$

The positional and orientational order of the Bragg and vortex-glass phases was characterized in real space by calculating the displacement correlator W^* and the orientational correlation function G_6 from the vortex positions observed by MD. In the main text data for the electron-irradiated samples A and B are shown. Here we show also the data for the pristine samples P for the range of fields $B/B_{\text{ord-dis}} < 1$ in which we have access to the structure with single vortex resolution by applying the MD technique. Results are consistent with data in the Bragg glass phase of electron irradiated samples: the orientational correlation function G_6 decays algebraically at intermediate and long-range and the displacement correlator $W^*(r)$ grows algebraically with distance as ex-

pected in the random manifold regime of the Bragg glass. The exponents of both algebraic evolutions with distance are shown in Fig. 4 (c) of the main text.

III. ACKNOWLEDGMENTS

This work was supported by the ECOS-Sud-MINCyt France-Argentina bilateral program under Grant A09E03; by the Argentinean National Science Foundation (ANPCyT) under Grants PRH-PICT 2008-294 and PICT 2011-1537; by the Universidad Nacional de Cuyo research grants program; and by Graduate Research fellowships from IB-CNEA for J. A. S and from Conicet for R. C. M., G. R. and N. R. C.B. We thank

to M. Li and A. Rykov for growing some of the studied pristine single crystals and V. Moser for providing us the Hall sensors.

IV. AUTHOR CONTRIBUTIONS

Y. F., A. P., M. K., and C. J. vd B. designed research; all authors performed research; J. A. S., Y. F. and A. P. analyzed data; Y. F. wrote the paper with the collaboration of the rest of the authors. The authors declare no conflict of interest.

*To whom correspondence should be addressed. E-mail: yanina.fasano@cab.cnea.gov.ar

-
- ¹ J. A. Mydosh, *Spin glasses*, Taylor & Francis, London, 1993.
 - ² C. C. Grimes, and G. Adams, Phys. Rev. Lett. **42**, 795, 1979.
 - ³ C. A. Murray, and D. H. Van Winkle, Phys. Rev. Lett. **58**, 1200 (1987).
 - ⁴ A. H. Marcus, and S. A. Rice, Phys. Rev. Lett. **77**, 2577 (1996).
 - ⁵ A. L. Thorneywork, J. L. Abbott, D. G. A. L. Aarts, and R. P. A. Dullens, Phys. Rev. Lett. **118**, 158001 (2017).
 - ⁶ H. M. Thomas, and G. E. Morfill, Nature **379**, 806 (1996).
 - ⁷ S. Deutschländer, T. Horn, H. Löwen, G. Maret, and P. Keim, Phys. Rev. Lett. **111**, 098301 (2013).
 - ⁸ J. M. Kosterlitz, and D. J. Thouless, J. Phys. C **6**, 1181 (1973).
 - ⁹ B. I. Halperin, and D. R. Nelson, Phys. Rev. Lett. **41**, 121 (1978).
 - ¹⁰ D. R. Nelson, and B. I. Halperin, Phys. Rev. B **19**, 2457 (1979).
 - ¹¹ A. P. Young, Phys. Rev. B **19**, 1855 (1979).
 - ¹² S. T. Chui, Phys. Rev. B **28**, 178 (1983).
 - ¹³ J. M. Kosterlitz, J. Phys. C **7**, 1046 (1974).
 - ¹⁴ G. Blatter, M. V. Feigel'man, V. B. Geshkenbein, A. I. Larkin and V. M. Vinokur, Rev. Mod. Phys. **66**, 1125 (1994).
 - ¹⁵ F. Pardo, F. de la Cruz, P. L. Gammel, E. Bucher and D. J. Bishop, Nature **396**, 348 (1998).
 - ¹⁶ A. Troyanovski, J. Aarts, and P. H. Kes, Nature (London) **399**, 665 (1999).
 - ¹⁷ M. Menghini, Y. Fasano, and F. de la Cruz, Phys. Rev. B **65**, 064510 (2002).
 - ¹⁸ Y. Fasano, M. Menghini, F. de la Cruz, Y. Paltiel, Y. Myasoedov, E. Zeldov, M. J. Higgins, and S. Bhattacharya, Phys. Rev. B **66**, R020512 (2002).
 - ¹⁹ A. P. Petrovic, Y. Fasano, R. Lortz, C. Senatore, A. Demuer, A. B. Antunes, A. Paré, D. Salloum, P. Gougeon, M. Potel, and Ø. Fischer, Phys. Rev. Lett. **103**, 257001 (2009).
 - ²⁰ I. Guillamón, R. Córdoba, J. Sesé, J. M. De Teresa, M. R. Ibarra, S. Vieira and H. Suderow, Nature Physics **10**, 851 (2014).
 - ²¹ M. Zehetmayer, Scientific Reports **5**, 9244 (2015).
 - ²² A. C. Ganguli, H. Singh, G. Saraswat, R. Ganguly, V. Bagwe, P. Shirage, A. Thamizhavel and P. Raychaudhuri, Scient. Reports **5**, 10613 (2015).
 - ²³ R. Toft-Petersen, A. B. Abrahamsen, S. Balog, L. Porcar and M. Laver, Nature Comm. **9**, 901 (2018).
 - ²⁴ T. Shibauchi, T. Nakano, M. Sato, T. Kisu, N. Kameda, N. Okuda, S. Ooi, and T. Tamegai, Phys. Rev. Lett. **83**, 1010 (1999).
 - ²⁵ M. B. Gaifullin, Yuji Matsuda, N. Chikumoto, J. Shimoyama, and K. Kishio, Phys. Rev. Lett. **84**, 2945 (2000).
 - ²⁶ T. Giamarchi and P. Le Doussal, Phys. Rev. B **52**, 1242 (1995).
 - ²⁷ T. Klein, I. Joumard, S. Blanchard, J. Marcus, R. Cubitt, T. Giamarchi, P. Le Doussal, Nature **413**, 404 (2001).
 - ²⁸ T. Nattermann and S. Scheidl, Adv. Phys. **49**, 607 (2000).
 - ²⁹ N. Avraham et al., Nature **411**, 451 (2001).
 - ³⁰ B. Khaykovich, M. Konczykowski, E. Zeldov, R. A. Doyle, T. Majer, P. H. Kes, and T. W. Li, Phys. Rev. B **56**, R517 (1997).
 - ³¹ V. M. Vinokur, B. Khaykovich, E. Zeldov, M. Konczykowski, R. A. Doyle and P. H. Kes, Phys. C **295**, 209 (1998).
 - ³² R. Cubitt, E. M. Forgan, G. Yang, S. L. Lee, D. M. Paul, H. A. Mook, M. Yethiraj, P. H. Kes, T. W. Li, A. A. Menovsky, Z. Tarnawski, and K. Mortensen, Nature **365**, 407 (1993).
 - ³³ H. Pastoriza, M. F. Goffman, A. Arribere and F. de la Cruz, Phys. Rev. Lett. **72**, 2951 (1994).
 - ³⁴ E. M. Forgan, M. T. Wylie, S. Lloyd, S. L. Lee, and R. Cubitt, Czech. Journal of Phys. **46**, 1571 (1996).
 - ³⁵ A. Pautrat, Ch. Simon, C. Goupil, P. Mathieu, A. Brûlet, C. D. Dewhurst, and A. I. Rykov, Phys. Rev. B **75**, 224512 (2007).
 - ³⁶ S. Demirdis, C. J. van der Beek, S. Mühlbauer, Y. Su and Th. Wolf, J. Phys. Condens. Matter **28**, 425701 (2016).
 - ³⁷ Y. Fasano, and M. Menghini, Supercond. Science and Tech. **21**, 023001 (2008).
 - ³⁸ M. Konczykowski, C. J. van der Beek, A. E. Koshelev, V. Mosser, M. Li, and P. H. Kes, Journal of Phys.: Conf. Series **150**, 052119 (2009).
 - ³⁹ Y. Fasano, M. De Seta, M. Menghini, H. Pastoriza, and F. de la Cruz, Proceedings of the Nat. Acad. Science **102**, 3898 (2005).
 - ⁴⁰ V. F. Correa, E. E. Kaul, and G. Nieva, Phys. Rev. B **63**,

- 172505 (2001).
- ⁴¹ F. Pardo, A. P. Mackenzie, F. de la Cruz, and J. Guimpel, Phys. Rev. B **55**, 14610 (1997).
 - ⁴² N. R. Cejas Bolecek, A. Kolton, M. Konczykowski, H. Pastoriza, D. Dominguez, and Y. Fasano, Phys. Rev. B **93**, 054505 (2016).
 - ⁴³ Y. Fasano, J. A. Herbsommer, F. de la Cruz, Phys. Stat. Sol. (b) **215**, 563 (1999).
 - ⁴⁴ R. Wördenweber and P. H. Kes, Phys. Rev. B **34**, 494 (1986).
 - ⁴⁵ E. M. Chyudnovsky, Phys. Rev. B **43**, 7831 (1991).
 - ⁴⁶ G. I. Menon, Phys. Rev. B **65**, 104527 (2002).
 - ⁴⁷ P. L. Gammel, U. Yaron, A. P. Ramirez, D. J. Bishop, A. M. Chang, R. Ruel, L. N. Pfeiffer, E. Bucher, G. D'Anna, D. A. Huse, K. Mortensen, M. R. Eskildsen and P. H. Kes, Phys. Rev. Lett. **80**, 833 (1998).
 - ⁴⁸ P. Kim, Z. Yao, C. A. Bolle and C. M. Lieber, Phys. Rev. B **60** R12589 (1995).
 - ⁴⁹ N. R. Cejas Bolecek, M. I. Dolz, H. Pastoriza, M. Konczykowski, C. J. van der Beek, A. B. Kolton, Y. Fasano, Phys. Rev. B **96**, 024507 (2017).
 - ⁵⁰ T. Giamarchi and S. Bhattacharya, in *Vortex Phases in "High Magnetic Fields: Applications in Condensed Matter Physics and Spectroscopy"*, edited by Berthier C *et al.* (Springer-Verlag, New York, 2002), Vol. 9, p. 314.
 - ⁵¹ H. Safar, P. L. Gammel, D. J. Bishop, D. B. Mitzi, and A. Kapitulnik, Phys. Rev. Lett. **68**, 2672 (1992).
 - ⁵² C. J. van der Beek, P. H. Kes, M. P. Maley, M. J. V. Menken, and A. A. Menovsky, Phys. C **195**, 307 (1992).
 - ⁵³ H. Beidenkopf, N. Avraham, Y. Myasoedov, H. Shtrikman, E. Zeldov, B. Rosenstein, E. H. Brandt, and T. Tamegai, Phys. Rev. Lett. **95**, 257004 (2005).
 - ⁵⁴ M. I. Dolz, Y. Fasano, H. Pastoriza, V. Mosser, M. Li, and M. Konczykowski, Phys. Rev. B **90**, 144507 (2014).
 - ⁵⁵ J. Gilchrist, and M. Konczykowski, Phys. C **212**, 43 (1993).
 - ⁵⁶ E. H. Brandt, Phys. Rev. Lett. **78**, 2208 (1997).

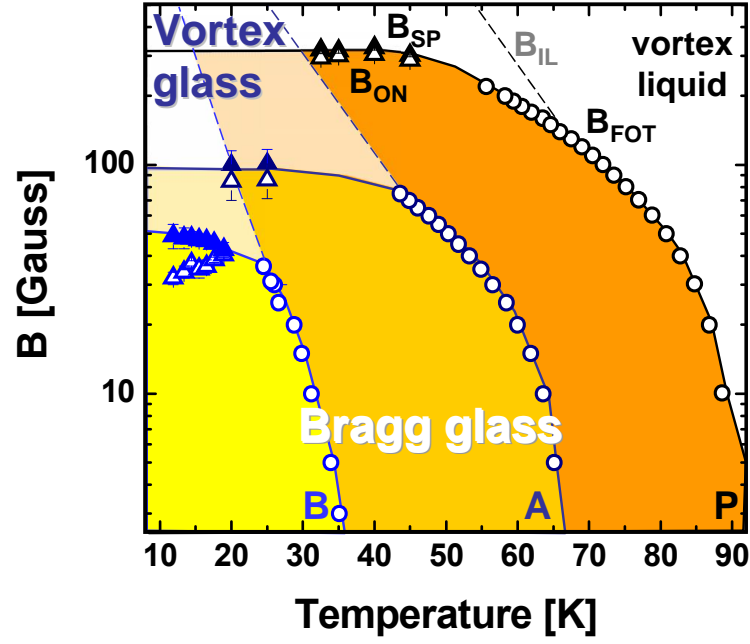


Figure 1: Vortex phase diagram for pristine (P) and electron-irradiated (A and B) $\text{Bi}_2\text{Sr}_2\text{CaCu}_2\text{O}_{8+\delta}$ samples from local dc and ac Hall magnetometry measurements. Sample A was irradiated with $1.7 \cdot 10^{19} \text{ e/cm}^2$ and sample B with $7.4 \cdot 10^{19} \text{ e/cm}^2$. First-order transition lines B_{FOT} (open circles) and $B_{\text{ord-dis}} = B_{\text{ON}}$ (open triangles) separate the Bragg glass from the vortex liquid phase at high temperatures, and the vortex glass at high fields. Full triangles signpost the location of the so-called second peak in the critical current B_{SP} . Dashed lines represent the irreversibility line B_{IL} , located very close to B_{FOT} for the fields at which the Bragg glass is stable. Solid lines are guides to the eye.

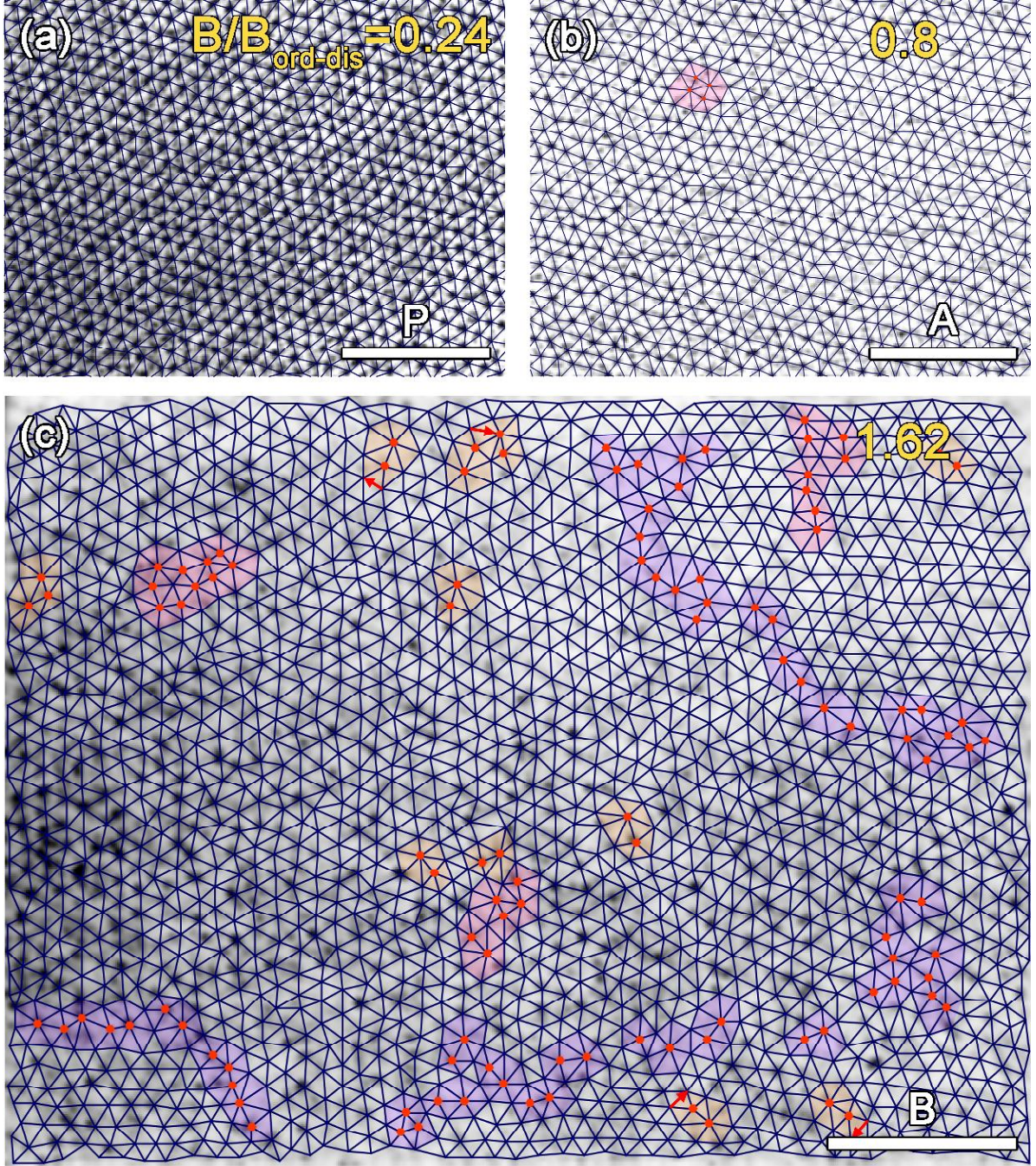


Figure 2: Magnetic decoration images of individual vortices (black dots) in the Bragg and the vortex glass phases of pristine (P) and electron-irradiated (A and B) $\text{Bi}_2\text{Sr}_2\text{CaCu}_2\text{O}_{8+\delta}$ samples. Vortex structures in the Bragg glass phase for (a) $B/B_{\text{ord-dis}} = 0.28$ in sample P and (b) $B/B_{\text{ord-dis}} = 0.8$ in sample A. (c) Large field-of-view snapshot of the vortex-glass phase observed in sample B for $B/B_{\text{ord-dis}} = 1.62$. Delaunay triangulations are superimposed on the structures: neighboring vortices are connected by dark blue lines and non-sixfold coordinated vortices are highlighted in red. Topological defects indicated with colors: grain boundaries highlighted in violet, edge dislocations in orange and twisted bonds in pink. Red arrows indicate the Burgers vectors of paired edge dislocations; no arrows are shown if dislocations seem to be unpaired in our experimental field-of-view. White bars indicate $5\ \mu\text{m}$.

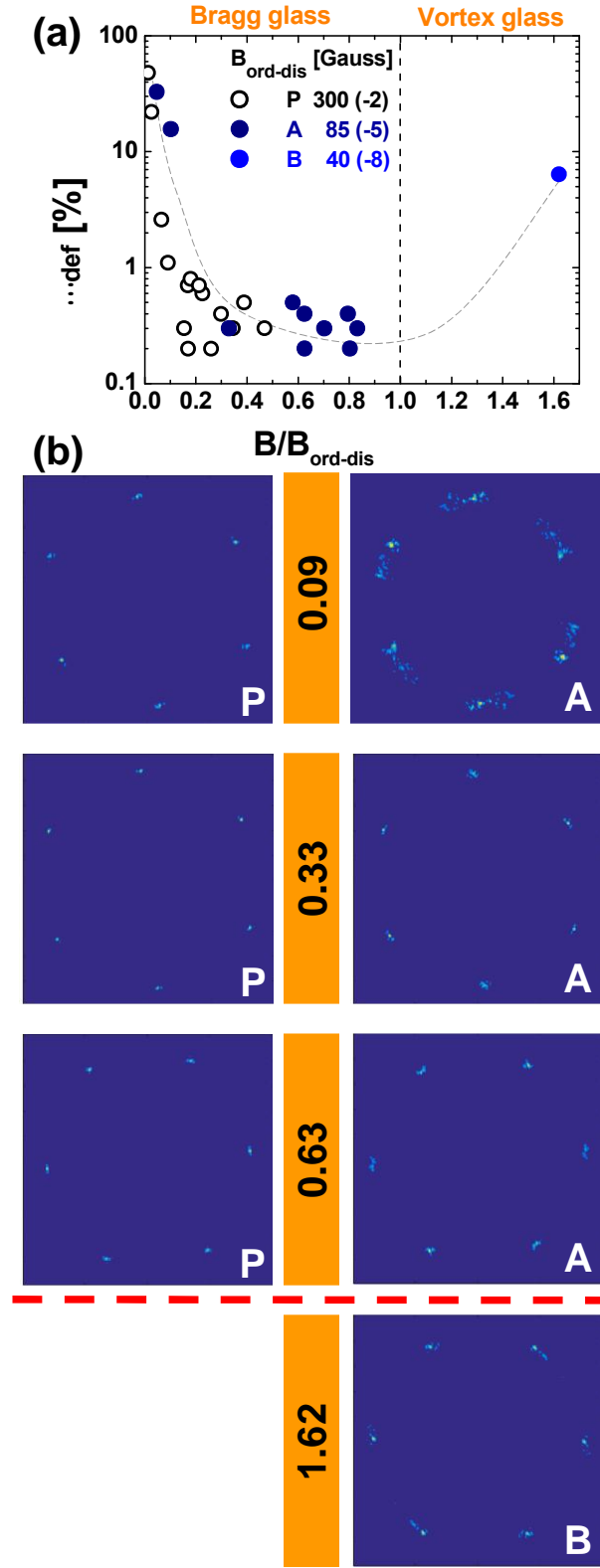


Figure 3: Topological defects and structure factor data for the Bragg and vortex glass phases of $\text{Bi}_2\text{Sr}_2\text{CaCu}_2\text{O}_{8+\delta}$ vortex matter at the surface of the samples. (a) Fraction of non-sixfold coordinated vortices, ρ_{def} , as a function of $B/B_{\text{ord-dis}}$. (b) Structure factor $S_{\text{MD}}(q, \Psi)$ of the vortex structure observed by magnetically decorating the individual vortex positions in pristine P (left panels) and electron-irradiated A and B (right panels) samples.

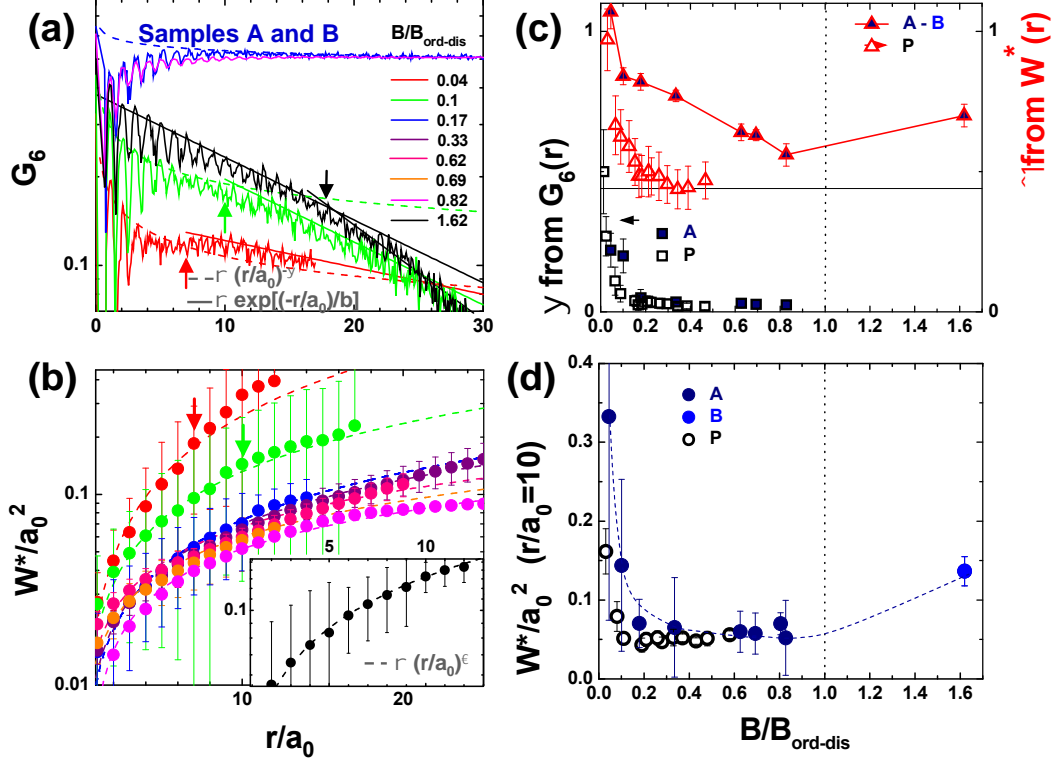


Figure 4: Orientational and positional order of the vortex and Bragg glass phases of $\text{Bi}_2\text{Sr}_2\text{CaCu}_2\text{O}_{8+\delta}$ vortex matter at the surface of electron-irradiated samples A and B. Data obtained from magnetic decoration experiments. (a) Orientational correlation function G_6 for various $B/B_{\text{ord-dis}}$. Arrows indicate the size of crystallites. (b) Displacement correlator W^*/a_0^2 calculated using the lanes algorithm avoiding the effect of topological defects. Data shown following the same color-code as in (a). Insert: detail of the fit for data obtained at $B/B_{\text{ord-dis}} = 1.62$. Dashed lines correspond to fits with an algebraic decay whereas full lines are exponential fits. (c) Exponents from the algebraic fittings of $G_6(r)$ (left axis, squares) and of $W^*(r)/a_0^2$ (right axis, triangles) for the Bragg and vortex glass phases of samples P, A and B. The dashed red line indicates the characteristic value of $\nu = 0.44$ expected for the random manifold regime. (d) Field-evolution of the displacement correlator at a fixed lattice spacing, $W^*(r/a_0 = 10)/a_0^2$.

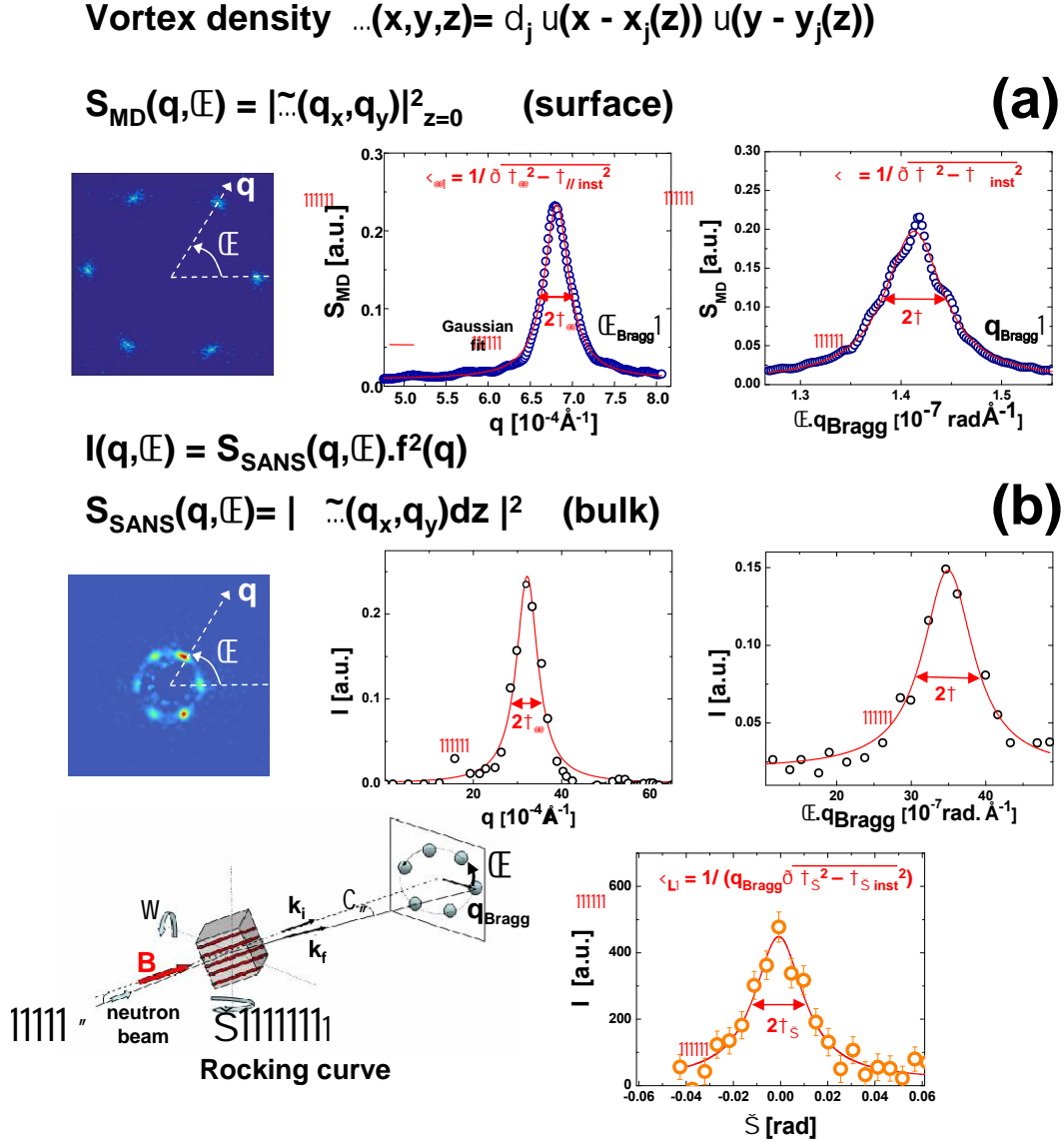


Figure 5: In-plane and along vortices correlation lengths as measured by small-angle neutron scattering (SANS) and magnetic decoration (MD) techniques. (a) Left: Structure factor at the sample surface obtained by imaging vortex positions with MD, $S_{MD}(q, \Psi)$ (sample P at $B/B_{ord-dis} = 0.15$). Middle: Radial q -profile of S_{MD} at a fixed Ψ on traversing a Bragg peak and calculation of the in-plane correlation length along the q direction, ξ_{\parallel}/a_0 . Right: azimuthal Ψ -profile of S_{MD} at q_{Bragg} and perpendicular in-plane correlation length ξ_{\perp}/a_0 . (b) Top left: Neutron diffraction pattern at Bragg condition (sample P at $B/B_{ord-dis} = 1.25$) proportional to the structure and the magnetic form factors of the vortex lattice $I(q, \Psi) = S_{SANS}(q, \Psi) \cdot f^2(q)$ at the whole volume of the sample. Top middle: radial q -profile of $I(q, \Psi)$ on traversing a Bragg peak. Top right: azimuthal Ψ -profile of $I(q, \Psi)$. Similarly as in the case of MD, fitting each profile with Gaussians yields the two in-plane correlation lengths ξ_{\parallel}/a_0 and ξ_{\perp}/a_0 . Bottom: experimental configuration and typical rocking-curve data from which the longitudinal correlation length, ξ_L/a_0 , can be extracted.

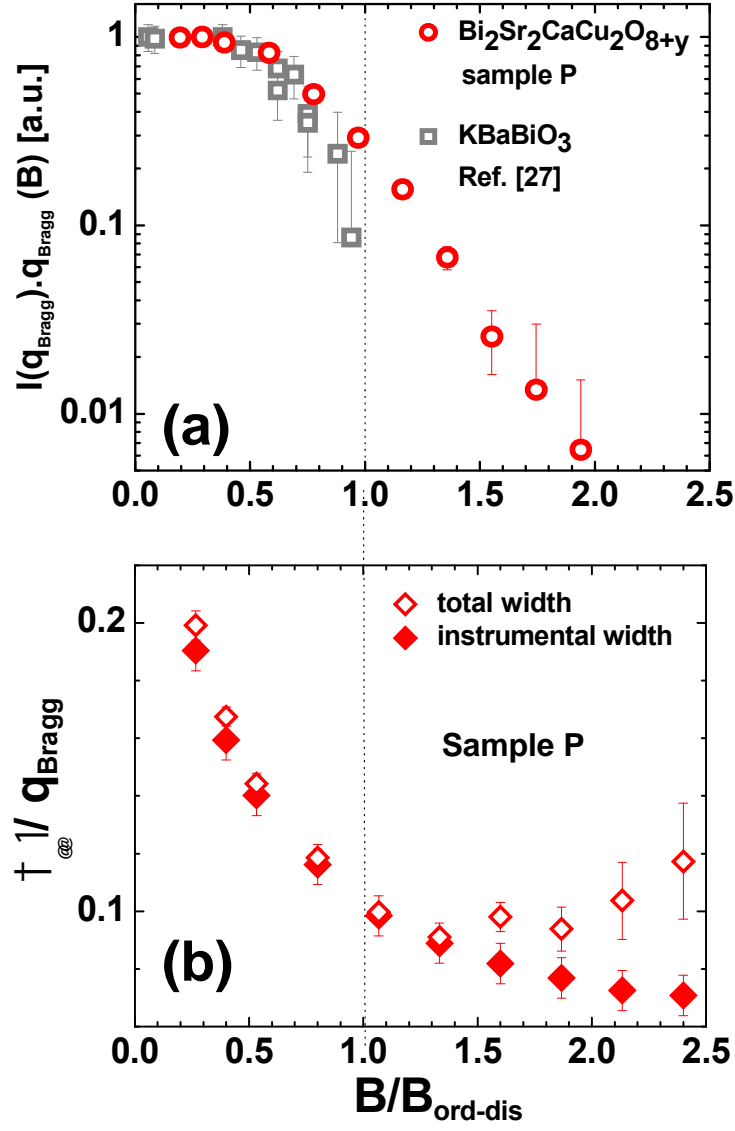


Figure 6: Neutron diffracted intensity (at $q = q_{\text{Bragg}}$) and width of the Bragg peaks as a function of $B/B_{\text{ord-dis}}$. (a) Normalized intensity in pristine $\text{Bi}_2\text{Sr}_2\text{CaCu}_2\text{O}_{8+\delta}$ (circles) compared to similar data in $(\text{K},\text{Ba})\text{BiO}_3$ (squares) taken from Ref. 27. (b) Average q -width of the Bragg peaks, $\sigma_{\parallel}/q_{\text{Bragg}}$, for pristine $\text{Bi}_2\text{Sr}_2\text{CaCu}_2\text{O}_{8+\delta}$ in comparison to our instrumental resolution.

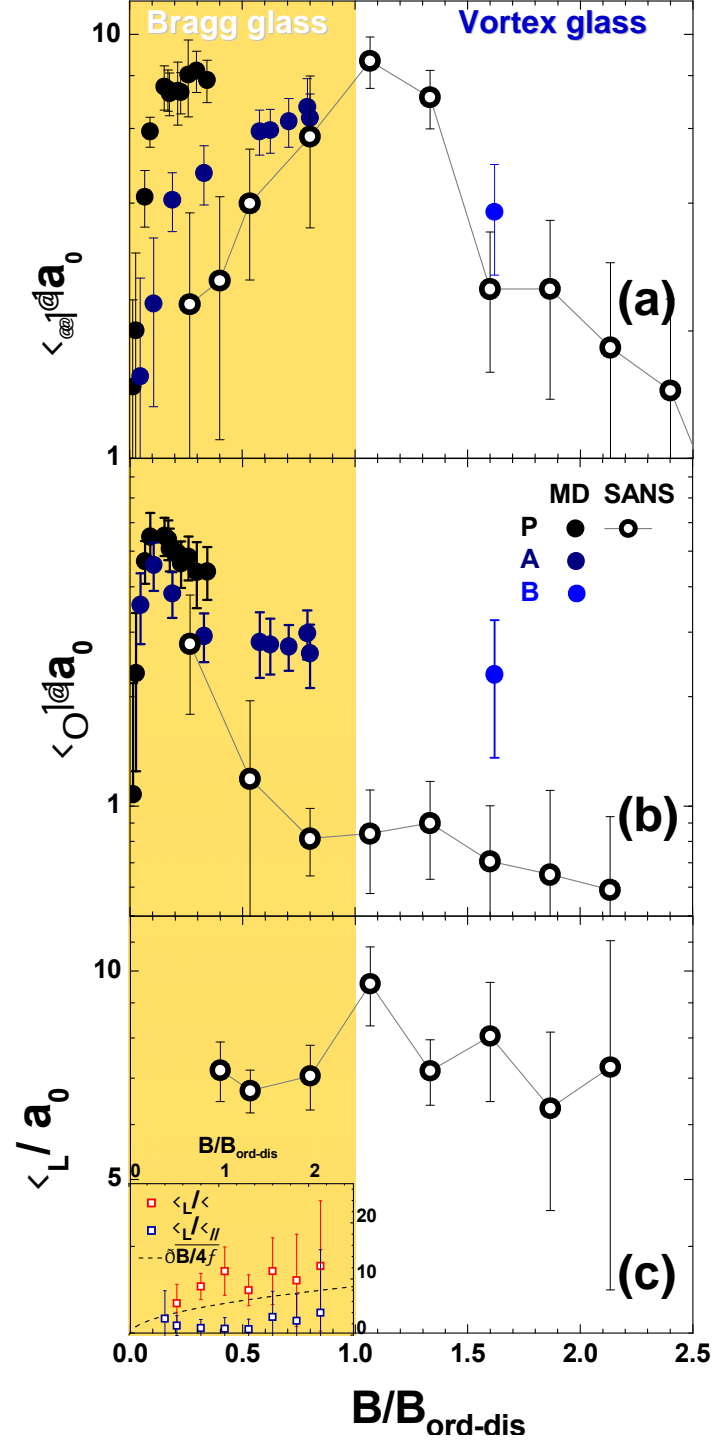


Figure 7: Field-evolution of the in-plane and longitudinal correlation lengths obtained from magnetic decoration (MD) data collected at the surface and small-angle-neutron-scattering (SANS) data probing vortex displacements along the sample thickness. Data for the Bragg and vortex glass phases in pristine samples P and electron-irradiated samples A and B. In-plane correlation lengths (a) parallel to the q -direction ξ_{\parallel}/a_0 and (b) along the azimuthal direction ξ_{\perp}/a_0 . (c) Longitudinal correlation length sensitive to the meandering of vortices along the field direction. Insert: Ratio between the longitudinal and in-plane correlation lengths obtained from SANS and comparison with the field-evolution of the bending energy term, $\sqrt{c_{44}/c_{66}} \sim \sqrt{B/4\pi}$, expected for $\text{Bi}_2\text{Sr}_2\text{CaCu}_2\text{O}_{8+\delta}$ (dashed line).

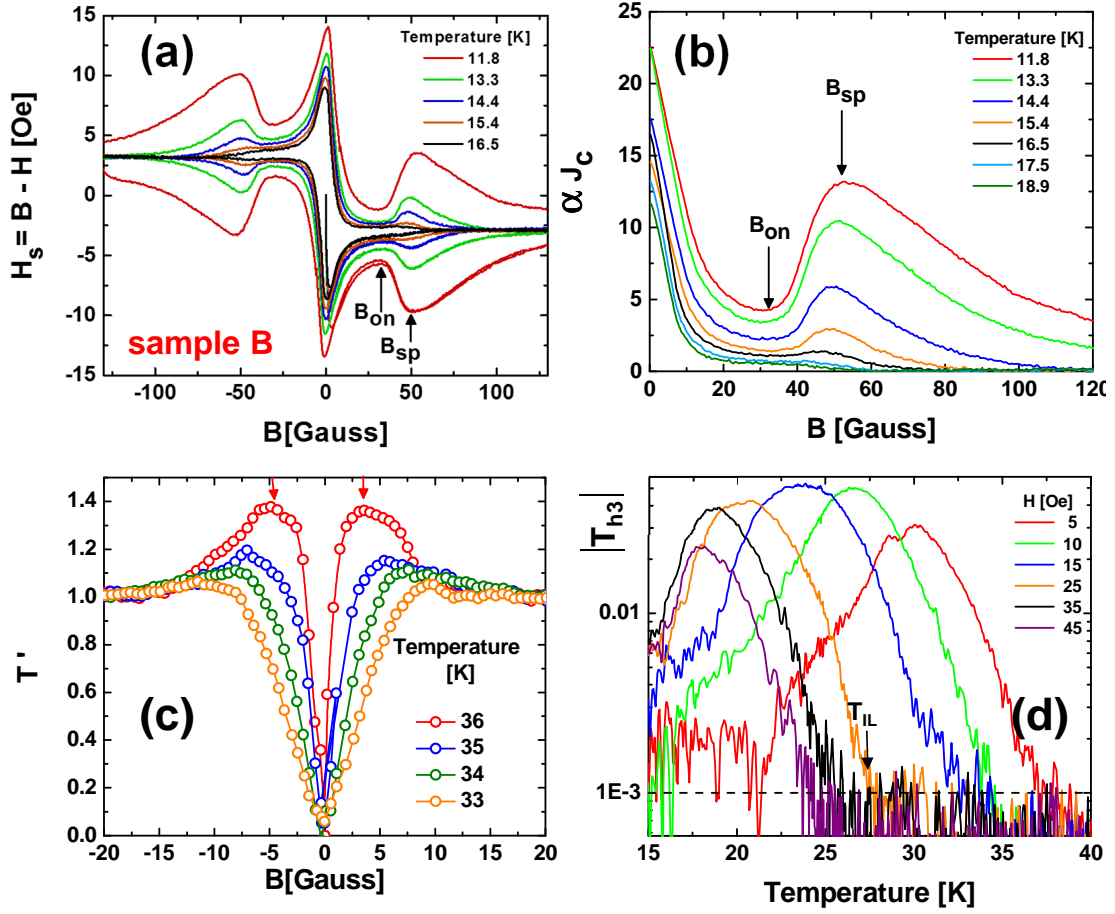


Figure 8: Detection of the vortex first-order transitions B_{FOT} (high temperatures) and $B_{\text{ord-dis}} = B_{\text{ON}}$ (low temperatures), and the irreversibility line for $\text{Bi}_2\text{Sr}_2\text{CaCu}_2\text{O}_{8+\delta}$. Data for the illustrative case of electron-irradiated sample B are obtained from local dc and ac magnetic measurements. (a) dc magnetization loops at low temperatures. (b) Separation of the ascending and descending branches of dc loops, proportional to the critical current J_c . Both figures highlight the field for the onset, B_{ON} , and full development, B_{SP} , of the peak in critical current, the former associated with the order-disorder transition. (c) Transmittivity loops at different temperatures in the high-temperature region showing paramagnetic peaks at B_{FOT} (see arrows). (d) Third harmonic signal presenting a non-negligible value when the magnetic response becomes non-linear at the irreversibility line H_{IL} (experimental noise indicated with a dotted line). ac measurements performed with a ripple field of 1 Oe in amplitude and frequency of 7.1 Hz.

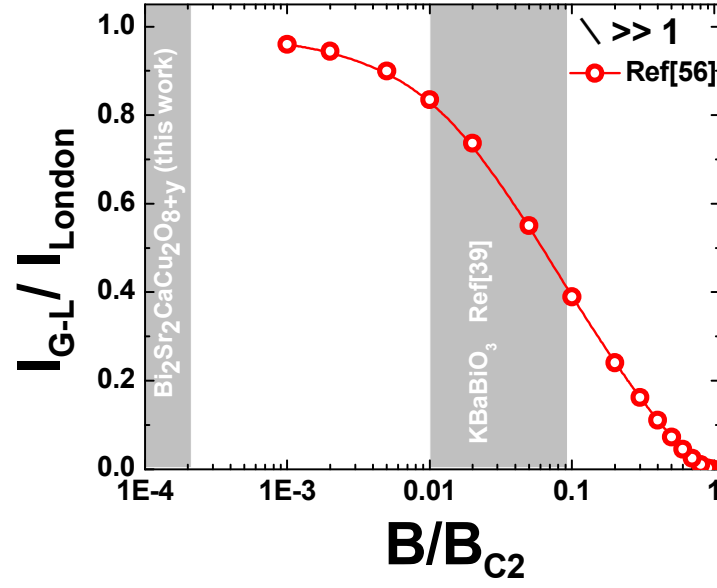


Figure 9: Ratio between the intensity of Bragg peaks in the Ginzburg-Landau and the London approximations, I_{G-L}/I_{London} , as a function of B/B_{c2} . This theoretical curve was calculated from Ref. 56. The light-gray regions indicate the field-ranges studied experimentally in $\text{Bi}_2\text{Sr}_2\text{CaCu}_2\text{O}_{8+\delta}$ in this work and in $(\text{K,Ba})\text{BiO}_3$ in Ref. 27.

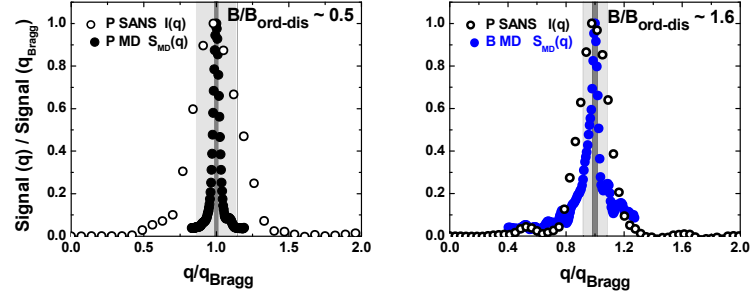


Figure 10: Comparison between the q -profiles of the normalized signals as observed by MD and SANS at the same $B/B_{\text{ord-dis}}$ below (left 0.4) and above (right 1.62) the order-disorder transition. The light-gray areas indicate the instrumental resolution of SANS data, mainly determined by the beam divergence and wavelength resolution. The dark-gray areas highlight the instrumental resolution of MD data.

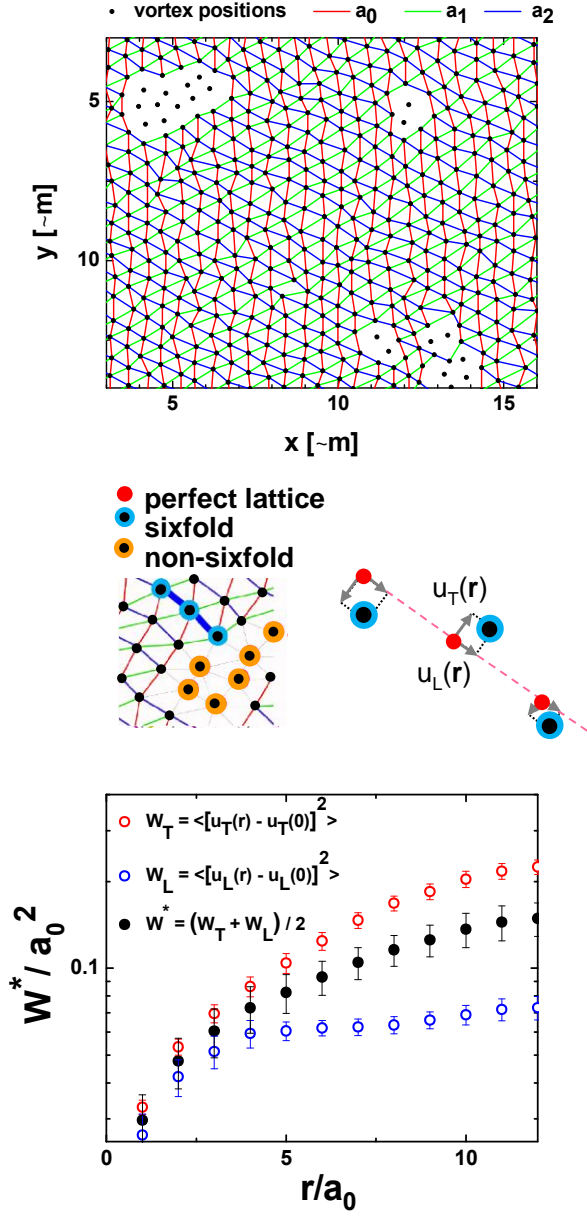


Figure 11: Top: Vortex positions and lanes considered to calculate the local vortex displacements $\mathbf{u}(\mathbf{r})$ with respect to the lattice sites along every avenue a_i (typical structure for the Bragg glass phase of the pristine sample P). Middle: Schematics of the vortex displacements computed to calculate the displacement correlator $W^*(r)$ along ($u_L(r)$) and perpendicular ($u_T(r)$) to a given lane at a distance r from its starting point. The positions of vortices are indicated with black dots with light-blue (orange) borders for sixfold (non-sixfold) coordinates vortices. The positions corresponding to the triangular lattice are shown in small red dots. Bottom: Transversal, longitudinal y total displacement correlators for this vortex structure as a function of r/a_0 .

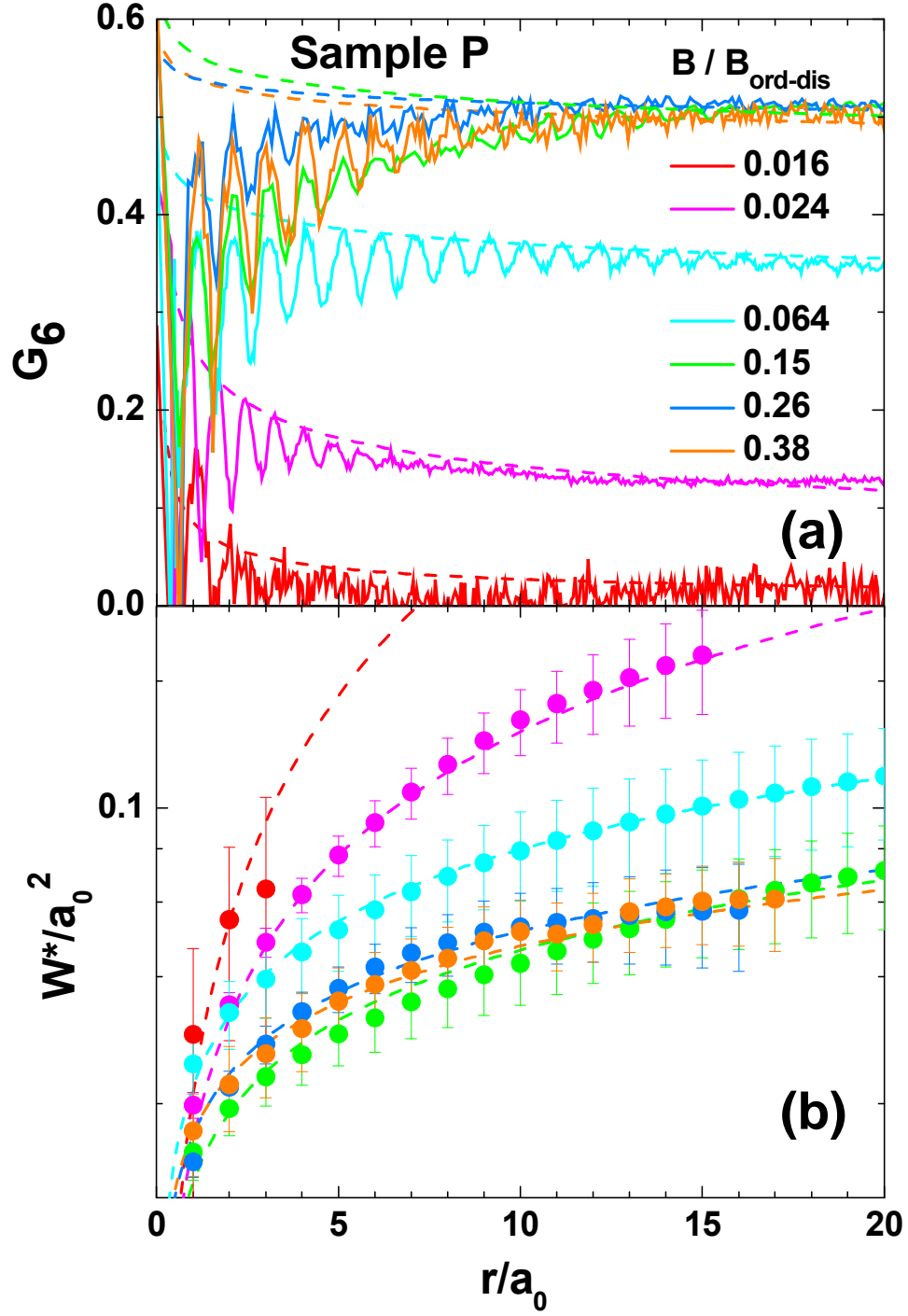


Figure 12: Orientational and positional order in the Bragg glass phase of pristine $\text{Bi}_2\text{Sr}_2\text{CaCu}_2\text{O}_{8+\delta}$ vortex matter. (a) Orientational correlation function G_6 for various $B/B_{\text{ord-dis}} < 1$. Dashed lines correspond to fits with an algebraic decay. (b) Displacement correlator W^*/a_0^2 calculated using the lanes algorithm (see text). Dashed lines: fits with an algebraic growth typical of the random manifold regime of the Bragg glass phase.